

# Quantum memory for microwave photons in an inhomogeneously broadened spin ensemble

Brian Julsgaard,<sup>1,\*</sup> Cécile Grezes,<sup>2</sup> Patrice Bertet,<sup>2</sup> and Klaus Mølmer<sup>1</sup>

<sup>1</sup>*Department of Physics and Astronomy, Aarhus University,  
Ny Munkegade 120, DK-8000 Aarhus C, Denmark.*

<sup>2</sup>*Quantronics group, SPEC (CNRS URA 2464), IRAMIS,  
DSM, CEA-Saclay, 91191 Gif-sur-Yvette, France*

(Dated: August 6, 2018)

We propose a multi-mode quantum memory protocol able to store the quantum state of the field in a microwave resonator into an ensemble of electronic spins. The stored information is protected against inhomogeneous broadening of the spin ensemble by spin-echo techniques resulting in memory times orders of magnitude longer than previously achieved. By calculating the evolution of the first and second moments of the spin-cavity system variables for realistic experimental parameters, we show that a memory based on NV center spins in diamond can store a qubit encoded on the  $|0\rangle$  and  $|1\rangle$  Fock states of the field with 80% fidelity.

PACS numbers: 03.67.Lx, 42.50.Ct, 42.50.Pq

Ensembles of electronic spins have been proposed as quantum memories in hybrid architectures for quantum computing including superconducting qubits [1–4]. Progress in this direction was reported in a number of experiments, demonstrating first strong coupling of an ensemble of spins in a crystal to a superconducting resonator [5–11], and more recently reversible storage of a single microwave photon in the spin ensemble [12, 13]. From these results it clearly appears that inhomogeneous broadening of the spin ensemble is a major obstacle, which needs to be overcome for hybrid quantum circuits to fully benefit from the long spin-coherence times. Due to inhomogeneous broadening, quantum information leaks from the "bright" collective degree of freedom coupled to the cavity into dark modes of the spin ensemble [14–16]. An appealing possibility is to actively and coherently restore it using refocusing techniques, inspired from magnetic-resonance methods [17] and based on the application of  $\pi$  pulses to the spins acting as time reversal. However, these ideas face a number of challenges: (i) The spatial inhomogeneity of the microwave resonator field may make it difficult to apply a  $\pi$  pulse efficiently to each spin, (ii) after the  $\pi$ -pulse inversion, the spin ensemble should remain stable despite its coupling to the cavity, and (iii) the whole statistics of the collective spin must be restored at the single quantum level. The present work proposes a protocol, which addresses all these issues, and we exemplify its feasibility for the specific case of NV centers in diamond [18], using currently available experimental techniques and realistic parameters. The proposed memory extends the storage times by several orders of magnitude compared to [12, 13]. It is intrinsically multi-mode and thus allows to store reversibly a number of quantum states, paving the way to the realization of a genuine quantum Turing machine [2, 19].

In our proposal the  $\pi$  pulses are performed by rapid adiabatic passage [20] through the electron spin reso-

nance, a method known to tolerate an inhomogeneous microwave field. Stability of the ensemble after inversion is ensured provided the cavity quality factor is sufficiently low [21]. Since this is incompatible with a faithful transfer of quantum information from the cavity into the spins, we propose to use a cavity with a quality factor that can be tuned in-between the steps of the protocol, as was recently demonstrated with SQUIDS [22]. In addition, inspired by a recent proposal of atomic-ensemble quantum memories for optical photons [23], we employ two  $\pi$  pulses in the refocusing scheme. To avoid emitting a microwave echo from the inverted spin ensemble, which would otherwise be more noisy than the original quantum state [24], we detune the cavity from the spins in-between the two pulses (effectively "silencing" this noisy first echo [23]). The second echo, formed in a non-inverted ensemble, restores quantum information with a fidelity up to 80 % for realistic parameters.

The proposed physical setup is shown schematically in Figs. 1(a) and (b); a diamond crystal containing NV centers [18] is placed on top of a transmission-wave-guide cavity whose frequency  $\omega_c$  [22] and coupling to the measuring line  $\kappa$  [25] can be tuned on a nanosecond timescale using control lines (not shown in Fig. 1). The crystal is subjected to a constant bias magnetic field  $\mathbf{B}_{\text{NV}}$ , lifting the degeneracy of the  $m_S = \pm 1$  states, and bringing the  $0 \rightarrow 1$  transition to an average frequency  $\omega_s = 2\pi \cdot 2.9$  GHz. In the frame rotating at  $\omega_s$  the free evolution of the cavity field and the spin ensemble is described by the Hamiltonian:  $\hat{H}_0 = \Delta_{\text{cs}} \hat{a}_c^\dagger \hat{a}_c + \sum_j \frac{\Delta_j}{2} \hat{\sigma}_z^{(j)}$ , where  $\hat{a}_c$  is the cavity field annihilation operator,  $\Delta_{\text{cs}} = \omega_c - \omega_s$  is the (adjustable) spin-cavity detuning,  $\Delta_j = \omega_j - \omega_s$ ,  $\omega_j$  the resonance frequency of the  $j$ th spin and  $\hat{\sigma}_z^{(j)}$  the corresponding Pauli operator. NV centers are coupled by hyperfine interaction to the nuclear spin of their nitrogen atom (having a spin 1), causing the  $m_S = 0 \rightarrow 1$  transition to split into a triplet separated by  $\Delta_{\text{hfs}}/2\pi =$

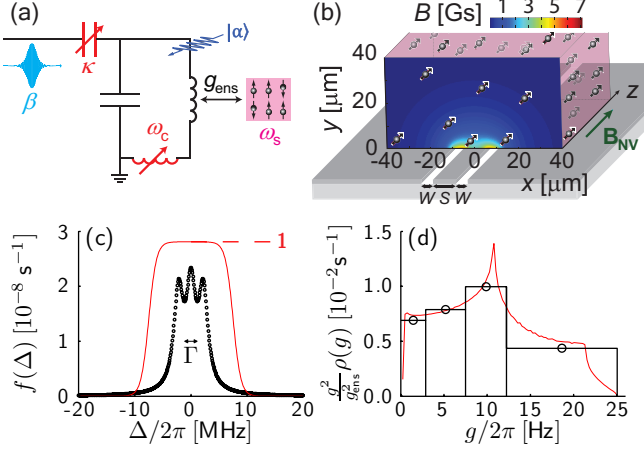


FIG. 1. (Color online) (a) Quantum memory circuit. The resonator, with frequency  $\omega_c$  and damping rate  $\kappa$  tunable at the nanosecond scale, is coupled to the spin ensemble (frequency  $\omega_s$ ) with an ensemble coupling constant  $g_{\text{ens}}$ . Drive pulses of amplitude  $\beta(t)$  are applied to the spins via the resonator, which can be initialized in a well-defined quantum state  $|\alpha\rangle$ . (b) Amplitude of the microwave field generated by a coplanar resonator with quality factor  $Q = 100$  and driven by a pulse of  $100 \mu\text{W}$  power. A static magnetic field  $\mathbf{B}_{\text{NV}}$  is applied parallel to the spins, which are distributed uniformly throughout the crystal. (c) Sub-ensemble distribution  $f(\Delta)$  of spin-resonance frequencies (circles) consisting of three hyperfine-split Lorentzian lines. The solid line shows the excitation probability for the chosen secant hyperbolic inversion pulses (see text). (d) (Solid line) Calculated coupling-strength distribution function  $\rho(g)g^2$ . (Histogram and circles) Sub-ensemble distribution used in the calculation. The low- and high-frequency cut-offs in  $\rho(g)$  originate from, respectively, high ( $40 \mu\text{m}$ ) and low ( $0.5 \mu\text{m}$ ) cut-offs in the distance from the resonator to NV centers.

2.2 MHz [26]. In addition, they are coupled by dipolar interactions to a bath of magnetic dipoles [27], which is known to govern their coherence time [28–30]. This bath broadens each of the hyperfine resonances, with a Lorentzian line shape [29] of width  $w$ , corresponding to a free-induction-decay time  $T_2^* = \frac{2}{w}$ . A Hahn-echo pulse sequence [17] partially refocuses this coherence, yielding a coherence time  $T_2$  which can be several orders of magnitude longer than  $T_2^*$ . In this work, we thus model the system by the static inhomogeneous spin distribution shown in Fig. 1(c) of characteristic width  $\Gamma \approx w$  [27], and damped at a rate  $\gamma_{\perp} = T_2^{-1}$  in the Markov approximation [27]. The spin-cavity interaction is described by:  $\hat{H}_I = \sum_j g_j (\hat{\sigma}_+^{(j)} \hat{a}_c + \hat{\sigma}_-^{(j)} \hat{a}_c^\dagger)$ , where the coupling constant  $g_j$  of the  $j$ th spin is distributed as shown in Fig. 1(d) [27]. This distribution is of no concern for storing the quantum state [12]; however, it prevents the application of a "hard"  $\pi$  pulse since each spin has a different Rabi frequency for a given drive amplitude. So-called hyperbolic secant pulses [31], where the pulse amplitude and phase are modulated as  $a_c = a_c^{\text{max}} [\text{sech}(\beta_{\text{sech}} t)]^{1+i\mu}$ ,

are known to remedy this issue [32]. The pulses are applied by an external drive  $\beta$  modeled by the Hamiltonian  $\hat{H}_{\text{ext}} = i\sqrt{2\kappa}(\beta \hat{a}_c^\dagger - \beta^* \hat{a}_c)$ . Note that to achieve the desired temporal dependence of  $\hat{a}_c$ ,  $\beta$  must be further tailored in order to account for the cavity filtering and the coupling to the spins [27].

The quantum memory protocol, shown schematically in Fig. 2(a), aims to store a cavity-field state given at  $t = 0$  and retrieve it again at  $t = T_{\text{mem}}$  with the cavity tuned to a "target frequency"  $\Delta_{\text{cs}}^t$ . This quantum state could be delivered by, e.g., a super-conducting transmon qubit along the lines of [12]. The cavity state is then transferred to the spins by setting  $\Delta_{\text{cs}} = 0$  for a time  $T_{\text{swap}}$  after which the cavity is parked at  $\Delta_{\text{cs}}^p$ . In a lowest-order approximation  $T_{\text{swap}} = \pi/2g_{\text{ens}}$  where  $g_{\text{ens}} = [\int g^2 \rho(g) dg]^{1/2}$  corresponds to the resonator-spin ensemble swap rate [12, 13, 16], but in reality is optimized numerically. For a high-fidelity storage, we set  $\kappa = \kappa_{\text{min}} = \frac{\omega_c}{2Q_{\text{max}}}$  with  $Q_{\text{max}} = 10^4$  so that the spin ensemble and resonator are in strong coupling. Next, in order to refocus the reversible spin dephasing we apply two  $\pi$  pulses at  $\sim \frac{T_{\text{mem}}}{4}$  and  $\sim \frac{3T_{\text{mem}}}{4}$  with  $\Delta_{\text{cs}} = 0$ , and to stabilize the inverted spin ensemble, we set  $\kappa = \kappa_{\text{max}} = \frac{\omega_c}{2Q_{\text{min}}}$  with  $Q_{\text{min}} = 100$  before the  $\pi$  pulses so that the cooperativity parameter fulfills  $C = \frac{g_{\text{ens}}^2}{\kappa\Gamma} < 1$  [21]. An additional constraint comes from the fact that tuning the cavity frequency or quality factor with SQUIDS is possible only if the cavity field is sufficiently low ( $|\langle \hat{a}_c \rangle| \lesssim 10$ ), which requires sufficient delay to allow it to decay after the  $\pi$  pulses. Between the two  $\pi$  pulses, we set  $\Delta_{\text{cs}} = \Delta_{\text{cs}}^p$  in order to silence the first spin echo [23]. After the second  $\pi$  pulse the quantum state is retrieved from the spin ensemble by setting  $\Delta_{\text{cs}} = 0$  during  $T_{\text{swap}}$  after which the cavity is tuned to  $\Delta_{\text{cs}}^t$ .

The numerical calculation of the dynamical evolution is made tractable by dividing the spins into  $M$  sub-ensembles along the lines of [21] keeping account of the mean values and covariances between cavity-field quadratures,  $\hat{X}_c$  and  $\hat{P}_c$ , and spin components,  $\hat{S}_x^{(m)}$ ,  $\hat{S}_y^{(m)}$ , and  $\hat{S}_z^{(m)}$  of the  $m$ th sub-ensemble [27]. Such a representation is convenient for determining the memory performance for, e.g., coherent input states. Specific for our NV-center example we use  $g_{\text{ens}} = 2\pi \cdot 3.5 \text{ MHz}$ ,  $w = 2\pi \cdot 2 \text{ MHz}$  corresponding to  $T_2^* = 0.16 \mu\text{s}$ ,  $T_2 = 100 \mu\text{s}$  [27], and hyperbolic secant  $\pi$  pulses truncated at a duration of  $1 \mu\text{s}$  with  $\mu = 3.5$  and  $\mu\beta_{\text{sech}} = 2\pi \cdot 7.5 \text{ MHz}$ . We assume that a microwave drive of peak power up to  $100 \mu\text{W}$  can be applied to the sample input without causing too much heating.

Typical results of our calculations are shown in Fig. 2. Panel (b) shows the mean values of  $\hat{X}_c$  and  $\hat{P}_c$  when a weak coherent cavity-field state is given at  $t = 0$ . Even though the cavity field is very strong during the inversion pulses at  $t \approx 2.5 \mu\text{s}$  and  $t \approx 7.5 \mu\text{s}$ , it relaxes to negligible levels prior to memory retrieval. Due to an

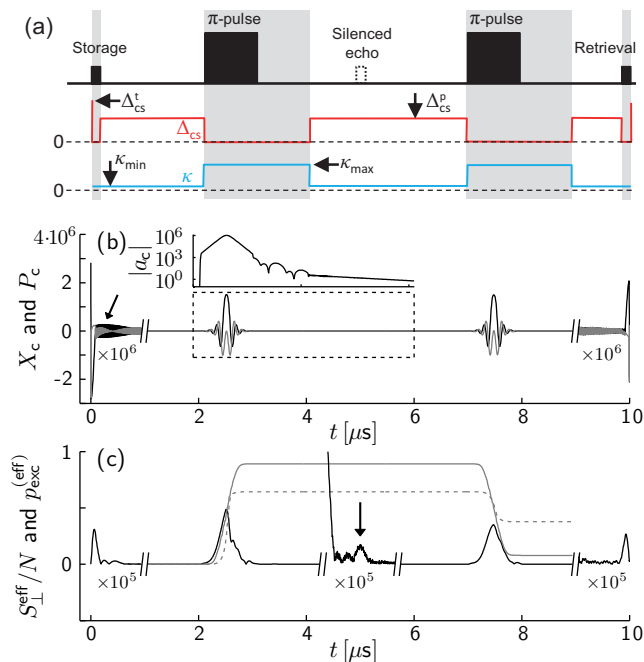


FIG. 2. (Color online) (a) Schematic timing of pulses and cavity parameters,  $\Delta_{cs}$  and  $\kappa$ . Periods of resonance ( $\Delta_{cs} = 0$ ) are marked by gray areas. (b) Cavity-field mean values,  $X_c$  (black) and  $P_c$  (gray) versus time. The inset re-plots the dashed-line region with  $|a_c|$  on the logarithmic vertical scale. (c) The  $g$ -weighted transverse-spin-component mean value  $S_{\perp}^{eff} = \sqrt{S_x^{eff 2} + S_y^{eff 2}}$  (black) normalized to  $N$ , the excitation probability  $p_{exc}$  (gray, dashed curve), and the  $g$ -weighted excitation probability  $p_{exc}^{eff}$  (gray, solid curve).

imperfect storage process [marked by the arrow in panel (b)] a minor part of the field is left in the cavity (14 % in field strength or 2 % in energy units), but most importantly  $|a_c|$  recovers at  $t = T_{mem}$  a value comparable to the one at  $t = 0$ . Regarding the spin state, we consider the *effective*,  $g$ -weighted spin observables,  $\hat{S}_{\eta}^{eff} = \sum_j \frac{g_j}{\bar{g}} \hat{\sigma}_{\eta}^{(j)}$ ,  $\eta = x, y$  and  $\bar{g} = g_{ens}/\sqrt{N}$ , which couple directly to the cavity field  $\hat{a}_c$  through the interaction Hamiltonian  $\hat{H}_I$ . Panel (c) shows the magnitude of these transverse spin components; in the storage part it grows as the quantum state is swapped from the cavity and then decays within  $T_2^*$  due to inhomogeneous broadening. Despite the excitation of very large mean spin components by the  $\pi$  pulses, the much weaker mean values of the stored spin states are recovered as a primary echo [arrow in panel (c)] and at the final memory retrieval. Panel (c) also shows the excitation probability  $p_{exc} = \frac{S_z + N}{2N}$  and the *effective*,  $g$ -weighted excitation probability  $p_{exc}^{eff} = \frac{1}{2N} (\sum_j \frac{g_j^2}{\bar{g}^2} \hat{\sigma}_z^{(j)} + N)$  versus time. The latter reaches 89 % between inversion pulses and levels off at 8 % after the second inversion pulse.

The above results can be extracted from mean-value equations alone and demonstrate the feasibility of the

spin ensemble as a classical memory. In order to assess the quantum properties of the memory we also calculate the evolution of variances by the coupled first- and second-moment equations detailed in the Supplementary Material [27], see Fig. 3. Panel (a) shows the summed variance of  $\hat{X}_c$  and  $\hat{P}_c$ , which deviates from the coherent-state value of unity during inversion pulses. At the memory retrieval the variance also increases when the cavity is tuned to resonance with  $Q = Q_{max}$  due to emission from spins left in the excited state by a non-perfect inversion process (in analogy to Ref. [24]), but most importantly this excess noise of only 11 % maintains easily the quantum nature of the memory. Panel (b) shows the summed variance of the spin components,  $\hat{S}_x^{eff}$  and  $\hat{S}_y^{eff}$ , which relaxes almost to the coherent-state value at the memory retrieval.

We stress the indispensable role of the spin-frequency inhomogeneity, which for a resonant cavity in low- $Q$  mode gives rise to the effective cooperativity parameter  $C = \frac{g_{ens}^2}{\kappa_{max} \Gamma} \approx 0.38$ . According to [21] this ensures (i) that the excess variance of  $\hat{X}_c$ ,  $\hat{P}_c$ ,  $\hat{S}_x^{eff}$ , and  $\hat{S}_y^{eff}$  converge to moderate, finite values during the resonant, inverted period (see, e.g., Fig. 3(a,b) at  $3 \mu s \lesssim t \lesssim 4 \mu s$ ), and (ii) that mean values of the coupled spin-cavity system observables relax sufficiently fast from possibly imperfect  $\pi$  pulses as exemplified in the inset of Fig. 2(b). For the off-resonant cavity the first and second moments of the spin components are damped on the  $T_2^*$  time scale as seen in Fig. 2(c) prior to the primary echo and in Fig. 3(b) at  $t \approx 4 \mu s$ , respectively. This is essential for the performance of the protocol; any reminiscence of the inversion pulses and excess noise in the spin ensemble must vanish both at the time of the primary echo and of the memory retrieval.

To assess the performance of the quantum memory, we repeat the above simulation with various other coherent input states. A selection of these are shown in Fig. 3(c) in terms of retrieved mean values and variances (gray circles) as compared to those of the input states (black circles). We confirm that the input/output relations constitute a linear map, which (i) essentially maps vacuum to vacuum (with a slightly increased variance) demonstrating that the remains of the inversion pulses are negligible and (ii) which presents a gain factor  $\mathcal{G} = 0.79$  for the mean values. The quadrature variances of the retrieved states amount to  $2\sigma^2 = \langle \delta \hat{X}_c^2 \rangle + \langle \delta \hat{P}_c^2 \rangle = 1.11$ . Since any quantum state can be expressed as a superposition of coherent states the memory should work for arbitrary input states, e.g. Schrödinger cats [33], and qubit states encoded in the  $|0\rangle$  and  $|1\rangle$  Fock states of the cavity. The storage time depends on the quantum state and the desired fidelity. Following [34] we obtain a qubit fidelity  $F_q = 80\%$  for  $T_{mem} = 10 \mu s$ .

To investigate the implications of the limited peak power available for inversion pulses, the above-mentioned

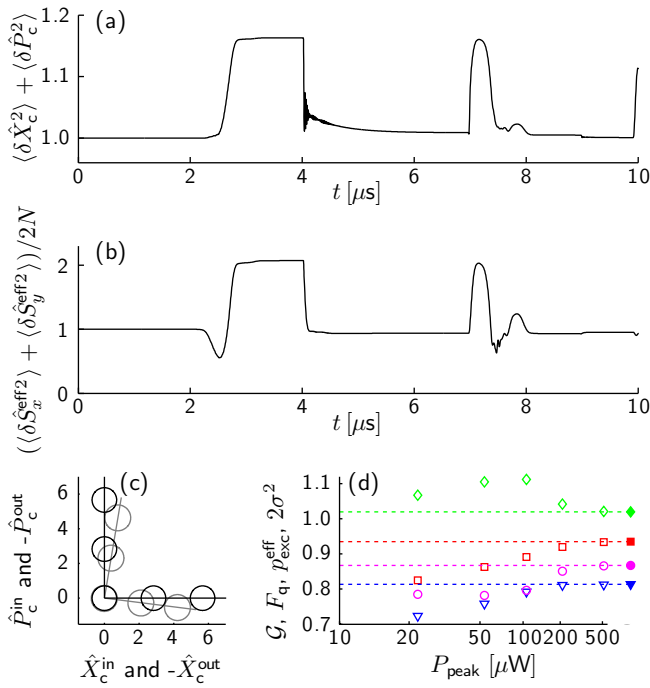


FIG. 3. (Color online) (a) Summed variance of cavity-field quadratures. (b) The summed,  $g$ -weighted spin-component variance normalized to  $2N$ . (c) Various input states (black) and output states (gray, sign reversed) examined in the protocol. The center of circles mark mean values whereas the radii mark the standard deviation  $\sigma$  of the state. (d) Open symbols: The dependence of gain  $\mathcal{G}$  (blue triangles), qubit fidelity  $F_q$  (magenta circles), effective excitation probability  $p_{\text{exc}}^{\text{eff}}$  (red squares), and summed variance  $2\sigma^2$  (green diamonds) on the peak power  $P_{\text{peak}}$  of the external driving field during inversion pulses. Closed symbols: Simulations with  $P_{\text{peak}} = 100 \mu\text{W}$  and homogeneous coupling  $g = 2\pi \cdot 12.5 \text{ Hz}$ , leading to  $\mathcal{G} = 0.82$ ,  $2\sigma^2 = 1.02$ , and  $F_q = 87\%$ .

analysis is repeated for a selection of peak powers ranging from  $20 \mu\text{W}$  to  $500 \mu\text{W}$  leading to the results presented in Fig. 3(d) with open symbols. Furthermore, a simulation is carried out at  $P_{\text{peak}} = 100 \mu\text{W}$  but with a homogeneous distribution of coupling strengths,  $g/2\pi = 12.5 \text{ Hz}$  (solid symbols in Fig. 3(d)). Clearly, increasing  $P_{\text{peak}}$  presents an increase in  $\mathcal{G}$  due to a better inversion process, but since in an intermediate regime a fraction of spins experiences a poor inversion process due to insufficient Rabi frequency (limiting the inversion performance illustrated by the dashed curve in Fig. 2(c)) we observe the non-monotonous behavior of  $2\sigma^2$  shown in Fig. 3(d). While increasing driving powers may be infeasible from an experimental point of view an alternative route to improvement lies in tailoring a more homogeneous distribution of coupling strengths, e.g. by limiting the distance between NV centers and the cavity.

Continuing the analysis with a homogeneous coupling-strength distribution (solid symbols in Fig. 3(d),  $F_q = 87\%$ ), we find the limiting factors for the obtained fidelity,

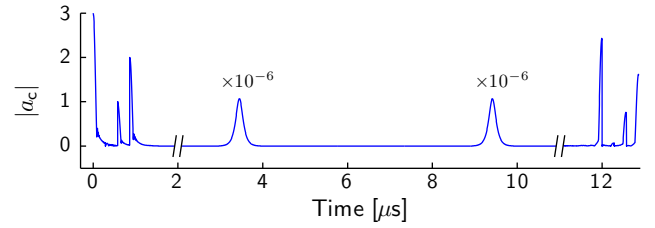


FIG. 4. (Color online) The cavity field  $|a_c|$  versus time in a multi-mode storage example with four input fields ( $|a_c| = 3, 0, 1, 2$ ) separated by  $0.29 \mu\text{s}$ , with memory time  $12 \mu\text{s}$ . The amplitude-cross-talk is below 3%.

which in terms of gain can be written approximately as:  $\mathcal{G} = \mathcal{G}_0 \exp(-\kappa[\frac{\pi}{2g_{\text{ens}}} + 2T_{\text{chirp}}]) \exp(-\gamma_{\perp}[T_{\text{mem}} - 0.7 \mu\text{s}])$ . The  $\kappa$ -dependent factor yields  $\approx 0.92$  due to cavity decay during the resonant swapping process and during the initial and final frequency chirp of duration  $T_{\text{chirp}}$ . The  $\gamma_{\perp}$ -dependent factor yields  $\approx 0.91$  due to spin decoherence (partly suppressed when the quantum state resides in the cavity or a population degree of freedom). The main contribution to excess noise arises from imperfect inversion processes, e.g. due to the dephasing rate  $\gamma_{\perp}$  during  $\pi$  pulses. In the limit  $T_2, Q_{\text{max}} \rightarrow \infty$  the qubit fidelity becomes  $\approx 97\%$ , and the origin of the remaining infidelity ( $\mathcal{G}_0 \approx 0.97$  and  $2\sigma^2 \approx 1.01$ ) includes a non-perfect cavity-to-spin transfer (arrow in Fig. 2(b)) and residual imperfections in the inversion processes.

As demonstrated experimentally for classical pulses [35], the spin-ensemble quantum memory is multi-mode in nature, which we confirm by simulating storage and retrieval of four pulses, see Fig. 4. The number of storage modes (proportional to  $T_2^*/T_2$ ) that can be faithfully addressed and refocused is estimated to be  $\sim 100$  [27].

In summary, a multi-mode spin-ensemble-based quantum memory for cavity fields has been proposed and analyzed for a specific realization using NV centers in diamond. With realistic experimental parameters a qubit fidelity of  $F_q = 80\%$  is predicted for  $T_{\text{mem}} = 10 \mu\text{s}$ . The main limiting processes are clarified, and we predict a qubit fidelity  $F_q > \frac{2}{3}$ , better than achieved by any classical strategy, for memory times of  $T_{\text{mem}} \lesssim 69 \mu\text{s}$ . The memory time may be further increased by dynamical decoupling techniques [36, 37] or quantum-state transfer to nuclear-magnetic degrees of freedom [38].

The authors acknowledge useful discussions with T. Chanelière, D. Esteve, and Y. Kubo and support from the EU integrated project AQUITE, the EU 7th Framework Programme collaborative project iQIT, and the ANR project QINVC (CHIST-ERA program).

\* brianj@phys.au.dk

[1] A. Imamoglu, Phys. Rev. Lett. **102**, 083602 (2009).

- [2] J. H. Wesenberg, A. Ardavan, G. A. D. Briggs, J. J. L. Morton, R. J. Schoelkopf, D. I. Schuster, and K. Mølmer, *Phys. Rev. Lett.* **103**, 070502 (2009).
- [3] D. Marcos, M. Wubs, J. M. Taylor, R. Aguado, M. D. Lukin, and A. S. Sørensen, *Phys. Rev. Lett.* **105**, 210501 (2010).
- [4] W. L. Yang, Z. Q. Yin, Y. Hu, M. Feng, and J. F. Du, *Phys. Rev. A* **84**, 010301R (2011).
- [5] Y. Kubo, F. R. Ong, P. Bertet, D. Vion, V. Jacques, D. Zheng, A. Dreau, J. F. Roch, A. Auffèves, F. Jelezko, J. Wrachtrup, M. F. Barthe, P. Bergonzo, and D. Esteve, *Phys. Rev. Lett.* **105**, 140502 (2010).
- [6] D. I. Schuster, A. P. Sears, E. Ginossar, L. DiCarlo, L. Frunzio, J. J. L. Morton, H. Wu, G. A. D. Briggs, B. B. Buckley, D. D. Awschalom, and R. J. Schoelkopf, *Phys. Rev. Lett.* **105**, 140501 (2010).
- [7] R. Amsüss, C. Koller, T. Nöbauer, S. Putz, S. Rotter, K. Sandner, S. Schneider, M. Schramböck, G. Steinhäuser, H. Ritsch, J. Schmiedmayer, and J. Majer, *Phys. Rev. Lett.* **107**, 060502 (2011).
- [8] M. U. Staudt, I.-C. Hoi, P. Krantz, M. Sandberg, M. Simoen, P. Bushev, N. Sangouard, M. Afzelius, V. S. Shumeiko, G. Johansson, P. Delsing, and C. M. Wilson, *J. Phys. B: At. Mol. Opt. Phys.* **45**, 124019 (2012).
- [9] H. Huebl, C. Zollitsch, J. Lotze, F. Hocke, M. Greifenstein, A. Marx, R. Gross, and S. T. B. Goennenwein, arXiv:1207.6039.
- [10] V. Ranjan, G. de Lange, R. Schutjens, T. Debelhoir, J. P. Groen, D. Szombati, D. J. Thoen, T. M. Klapwijk, R. Hanson, and L. DiCarlo, arXiv:1208.5473.
- [11] S. Probst, H. Rotzinger, S. Wünsch, P. Jung, M. Jerger, M. Siegel, A. V. Ustinov, and P. A. Bushev, arXiv:1212.2856.
- [12] Y. Kubo, C. Grezes, A. Dewes, T. Umeda, J. Isoya, H. Sumiya, N. Morishita, H. Abe, S. Onoda, T. Ohshima, V. Jacques, A. Dréau, J.-F. Roch, I. Diniz, A. Auffèves, D. Vion, D. Esteve, and P. Bertet, *Phys. Rev. Lett.* **107**, 220501 (2011).
- [13] X. Zhu, S. Saito, A. Kemp, K. Kakuyanagi, S.-i. Karimoto, H. Nakano, W. J. Munro, Y. Tokura, M. S. Everitt, K. Nemoto, M. Kasu, N. Mizuochi, and K. Semba, *Nature* **478**, 221 (2011).
- [14] Z. Kurucz, J. H. Wesenberg, and K. Mølmer, *Phys. Rev. A* **83**, 053852 (2011).
- [15] I. Diniz, S. Portolan, R. Ferreira, J. M. Gérard, P. Bertet, and A. Auffèves, *Phys. Rev. A* **84**, 063810 (2011).
- [16] Y. Kubo, I. Diniz, A. Dewes, V. Jacques, A. Dréau, J.-F. Roch, A. Auffèves, D. Vion, D. Esteve, and P. Bertet, *Phys. Rev. A* **85**, 012333 (2012).
- [17] E. L. Hahn, *Phys. Rev.* **80**, 580 (1950).
- [18] A. Gruber, A. Dräbenstedt, C. Tietz, L. Fleury, J. Wrachtrup, and C. von Borczyskowski, *Science* **276**, 2012 (1997).
- [19] K. Tordrup, A. Negretti, and K. Mølmer, *Phys. Rev. Lett.* **101**, 040501 (2008).
- [20] A. Abragam, *The principles of nuclear magnetism* (Clarendon Press, Oxford, 1961).
- [21] B. Julsgaard and K. Mølmer, *Phys. Rev. A* **86**, 063810 (2012).
- [22] A. Palacios-Laloy, F. Nguyen, F. Mallet, P. Bertet, D. Vion, and D. Esteve, *J. Low Temp. Phys.* **151**, 1034 (2008).
- [23] V. Damon, M. Bonarota, A. Louchet-Chauvet, T. Chanelière, and J.-L. Le Gouët, *New J. Phys.* **13**, 093031 (2011).
- [24] J. Ruggiero, J.-L. Le Gouët, C. Simon, and T. Chanelière, *Phys. Rev. A* **79**, 053851 (2009).
- [25] Y. Yin, Y. Chen, D. Sank, P. J. J. O'Malley, T. C. White, R. Barends, J. Kelly, E. Lucero, M. Mariantoni, A. Megrant, C. Neill, A. Vainsencher, J. Wenner, A. N. Korotkov, A. N. Cleland, and J. M. Martinis, arXiv:1208.2950.
- [26] S. Felton, A. M. Edmonds, M. E. Newton, P. M. Martineau, D. Fisher, D. J. Twitchen, and J. M. Baker, *Phys. Rev. B* **79**, 075203 (2009).
- [27] "See supplementary material for details."
- [28] R. Hanson, V. V. Dobrovitski, A. E. Feiguin, O. Gywat, and D. D. Awschalom, *Science* **320**, 352 (2008).
- [29] V. V. Dobrovitski, A. E. Feiguin, D. D. Awschalom, and R. Hanson, *Phys. Rev. B* **77**, 245212 (2008).
- [30] N. Zhao, S.-W. Ho, and R.-B. Liu, *Phys. Rev. B* **85**, 115303 (2012).
- [31] M. S. Silver, R. I. Joseph, and D. I. Hoult, *Phys. Rev. A* **31**, R2753 (1985).
- [32] M. Garwood and L. DelaBarre, *J. Mag. Res.* **153**, 155 (2001).
- [33] H. Wang, M. Hofheinz, M. Ansmann, R. C. Bialczak, E. Lucero, M. Neeley, A. D. OConnell, D. Sank, M. Weides, J. Wenner, A. N. Cleland, and J. M. Martinis, *Phys. Rev. Lett.* **103**, 200404 (2009).
- [34] J. F. Sherson, H. Krauter, R. K. Olsson, B. Julsgaard, K. Hammerer, I. Cirac, and E. S. Polzik, *Nature* **443**, 557 (2006).
- [35] H. Wu, R. E. George, J. H. Wesenberg, K. Mølmer, D. I. Schuster, R. J. Schoelkopf, K. M. Itoh, A. Ardavan, J. J. L. Morton, and G. A. D. Briggs, *Phys. Rev. Lett.* **105**, 140503 (2010).
- [36] G. de Lange, Z. H. Wang, D. Ristè, V. V. Dobrovitski, and R. Hanson, *Science* **330**, 60 (2010).
- [37] N. Bar-Gill, L. M. Pham, A. Jarmola, D. Budker, and R. L. Walsworth, arXiv:1211.7094.
- [38] G. D. Fuchs, G. Burkard, P. V. Klimov, and D. D. Awschalom, *Nature Phys.* **7**, 789 (2011).

## SUPPLEMENTARY MATERIAL

### The effective spin- $\frac{1}{2}$ Hamiltonian

The interaction Hamiltonian between the spin state of NV centers and the microwave cavity field is calculated in the following. The electronic part of the Hamiltonian for a single NV-center in an external magnetic field reads:

$$\hat{H} = D\hat{S}_z^2 + E(\hat{S}_x^2 - \hat{S}_y^2) + g_{\text{NV}}\mu_{\text{B}}\hat{\mathbf{S}} \cdot \hat{\mathbf{B}}, \quad (1)$$

where  $D = 2\pi \cdot 2.88$  GHz is the zero-field splitting between the  $m_S = 0$  and  $m_S = \pm 1$  states,  $E$  is a splitting between the  $m_S = \pm 1$  states induced by non-axial strain [1],  $g_{\text{NV}} = 2$  is the gyro-magnetic ratio,  $\mu_{\text{B}}$  is the Bohr magneton,  $\hat{\mathbf{S}}$  is the real spin (not to be confused with the collective ensemble-spin  $\hat{\mathbf{S}}$  defined elsewhere in the manuscript), and  $\hat{\mathbf{B}}$  is the external magnetic field. The NV-center axis defines the direction of quantization along  $z$ , which we assume in this work to be parallel to the sample.

The NV center is effectively reduced to a two-level system by applying a static bias magnetic field  $B_z$ . If the Zeeman energy verifies  $g_{\text{NV}}\mu_{\text{B}}B_z \gg E$ , which is the case for  $B \geq 0.5$  mT, the spin states  $m_S = 0, \pm 1$  are also energy eigen states. Taking as our ground state  $|g\rangle = |m_S = 0\rangle$  and excited state  $|e\rangle = |m_S = 1\rangle$ , the transition energy becomes:  $\omega = D + g_{\text{NV}}\mu_{\text{B}}B_z + O\left(\frac{E^2}{g_{\text{NV}}\mu_{\text{B}}B_z}\right)$ . As will be detailed below, the quantized cavity field is linearly polarized within the  $xy$ -plane and can be written:  $\hat{\mathbf{B}} = \delta\mathbf{B}(\hat{a}_c + \hat{a}_c^\dagger)$ . In perturbation theory the interaction part of the Hamiltonian then reads:

$$\begin{aligned} \hat{H}_{\text{I}} &= g_{\text{NV}}\mu_{\text{B}} \left[ \hat{S}_x \delta B_x(\mathbf{r}) + \hat{S}_y \delta B_y(\mathbf{r}) \right] (\hat{a}_c + \hat{a}_c^\dagger) \\ &= \frac{g_{\text{NV}}\mu_{\text{B}}}{2} \left[ \hat{S}_+ \{ \delta B_x(\mathbf{r}) - i\delta B_y(\mathbf{r}) \} + \hat{S}_- \{ \delta B_x(\mathbf{r}) + i\delta B_y(\mathbf{r}) \} \right] (\hat{a}_c + \hat{a}_c^\dagger) \\ &= \frac{g_{\text{NV}}\mu_{\text{B}}}{\sqrt{2}} \left[ \hat{a}_c \hat{\sigma}_+ \{ \delta B_x(\mathbf{r}) - i\delta B_y(\mathbf{r}) \} + \hat{a}_c^\dagger \hat{\sigma}_- \{ \delta B_x(\mathbf{r}) + i\delta B_y(\mathbf{r}) \} \right] \\ &\rightarrow \frac{g_{\text{NV}}\mu_{\text{B}} |\delta\mathbf{B}_\perp(\mathbf{r})|}{\sqrt{2}} \left[ \hat{a}_c \hat{\sigma}_+ + \hat{a}_c^\dagger \hat{\sigma}_- \right]. \end{aligned} \quad (2)$$

The second line uses the standard definition of raising- and lowering operators,  $\hat{S}_\pm = \hat{S}_x \pm i\hat{S}_y$ , with properties:  $\hat{S}_\pm |m_S\rangle = \sqrt{\mathcal{S}(\mathcal{S} + 1) - m_S(m_S \pm 1)} |m_S \pm 1\rangle$ . Restricted to our effective two-level system,  $|g\rangle$  and  $|e\rangle$ , these operators can be stated in terms of Pauli operators:  $\hat{S}_\pm = \sqrt{2}\hat{\sigma}_\pm$ , which has been exploited in the third line together with the rotating-wave approximation. The last expression is obtained by writing  $\delta B_x(\mathbf{r}) + i\delta B_y(\mathbf{r}) = |\delta\mathbf{B}_\perp(\mathbf{r})|e^{i\theta(\mathbf{r})}$

and re-defining our basis states as  $|g\rangle$  and  $e^{-i\theta(\mathbf{r})}|e\rangle$  (such that the phase factor is absorbed into  $\hat{\sigma}_\pm$ ). We conclude that the coupling between the cavity field and the effective spin- $\frac{1}{2}$  of the  $j$ th NV center located at  $\mathbf{r}_j$  is given by:

$$g_j = \frac{g_{\text{NV}}\mu_{\text{B}}|\delta\mathbf{B}_\perp(\mathbf{r}_j)|}{\sqrt{2}}. \quad (3)$$

Analytical expressions for the magnetic field of a wave traveling in the  $z$  direction along a coplanar transmission line of the geometry, shown in Fig. 1(b) of the main text, can be expressed as a function of the voltage  $V_0$  between the center conductor and the ground plane [2]:

$$\begin{aligned} B_x &= -\frac{2\mu_0 V_0}{\eta b} \sqrt{\epsilon_{\text{eff}}} \sum_{n=1}^{\infty} \frac{1}{F_n} \left[ \frac{\sin n\pi\delta/2}{n\pi\delta/2} \sin \frac{n\pi\bar{\delta}}{2} \right] \cos \frac{n\pi x}{b} e^{-\gamma_n y}, \\ B_y &= -\frac{2\mu_0 V_0}{\eta b} \sqrt{\epsilon_{\text{eff}}} \sum_{n=1}^{\infty} \left[ \frac{\sin n\pi\delta/2}{n\pi\delta/2} \sin \frac{n\pi\bar{\delta}}{2} \right] \sin \frac{n\pi x}{b} e^{-\gamma_n y}, \\ \gamma_n &= \sqrt{\left(\frac{n\pi}{b}\right)^2 + \left(\frac{4\pi cb\sqrt{\epsilon_{\text{eff}} - 1}}{n\omega_c}\right)^2}. \end{aligned} \quad (4)$$

In this expression,  $\mu_0$  is the vacuum permeability,  $\eta = 376.7$  the vacuum impedance,  $c$  the speed of light,  $\epsilon_{\text{eff}} = (\epsilon_r + 1)/2$ ,  $\epsilon_r$  being the relative dielectric constant of the substrate, and  $\delta = W/b$ ,  $\bar{\delta} = (S + W)/b$ ,  $F_n = \frac{b\gamma_n}{n\pi}$  are geometrical quantities with  $S$  the width of the coplanar waveguide central conductor,  $W$  its distance to each ground plane [see Fig. 1(b) of the main text], and  $b$  the ground plane width.

In a  $\lambda/2$  coplanar waveguide resonator of length  $L$  defined by a transmission line open at  $z = 0$  and  $z = L$ , the fields are generated by voltages and currents  $V(z) = V(0) \cos(\pi z/L)$  and  $I(z) = -iV(0) \sin(\pi z/L)/Z_0$ , so that the current in the middle of the transmission line verifies  $I(L/2) = iV(L)/Z_0$ , the same relation as between the current and voltage of a traveling microwave at a given position of a coplanar waveguide. The zero-point rms fluctuations of the magnetic field in the middle of the resonator are thus directly obtained by replacing in the previous expressions  $V_0$  by the zero-point rms fluctuations of the voltage at the resonator end  $\delta V_0(L) = \omega_c \sqrt{\hbar Z_0/\pi}$  [3]. In this work we chose the waveguide geometry so that  $Z_0 = 50\Omega$ , as was the case in a number of recent experiments [4].

Using the expression for the rms zero-point magnetic field fluctuations, we obtain the dependence of the coupling constant of a spin located in the middle of the resonator ( $z = L/2$ ) as a function of  $x, y$ . From that we calculate the coupling constant distribution shown in Fig. 1(d) of the main text.

## The electron-spin-resonance transition of the NV ensemble

We now discuss the spin lineshape and coherence properties that were chosen in the main text. The electronic spin of all NV centers is also coupled by hyperfine interaction to the nuclear spin of the nitrogen atom. This leads to an additional structure of the electron spin resonance. In the case of NV centers with a  $^{14}\text{N}$  nucleus as is the case with diamond samples prepared with natural nitrogen abundance, the spectrum is known to consist of three peaks separated by  $\Delta_{\text{hfs}}/2\pi = 2.2\text{ MHz}$  [5].

In addition to the hyperfine coupling to the nitrogen nucleus, NV centers are coupled to a bath of other spins that determines their coherence properties, namely the line width and the spin echo time  $T_2$ . Two different well-identified spin baths contribute to NV center decoherence: nitrogen impurities (so-called P1 centers), and  $^{13}\text{C}$  nuclear spins. Hybrid circuit experiments usually require a rather high concentration in NV centers (typically 1 ppm or more), in order to efficiently absorb single photons or equivalently to reach the strong coupling regime. This high concentration also implies a comparatively large concentration of P1 centers (on the order of a few ppm), which at this level are mostly responsible for the sample coherence properties [6]. A sample with  $[\text{NV}] \sim 2\text{ ppm}$  and  $[\text{P1}] \sim 2\text{ ppm}$  can be achieved with usual crystal preparation techniques (electron irradiation of a nitrogen-doped crystal). According to [6], such a sample would have a line width of each of the hyperfine peaks around  $w/2\pi = 0.5\text{ MHz}$ , a spin-echo coherence time  $T_2 \sim 100\ \mu\text{s}$ , and according to [7] would be coupled to a coplanar resonator with an ensemble coupling constant  $g_{\text{ens}}/2\pi \sim 3\text{ MHz}$ . These are parameters similar to the ones we use in our calculations (see main text), apart for the line width which we take somewhat broader  $w/2\pi = 2\text{ MHz}$ . Broadening the line width purposely could easily be achieved, either by adding a slightly inhomogeneous magnetic field, or by a slight misalignment of the magnetic field with a crystalline axis, which results in a slight difference in Zeeman shift for NV centers with different orientation [7]. We finally note that in order to avoid complications of Electron Spin Echo Envelope Modulation (ESEEM) caused by the interaction with the bath of  $^{13}\text{C}$  nuclei [8], it would be preferable to use a  $^{12}\text{C}$ -isotope-enriched diamond crystal for this experiment. With a sample having natural abundance of  $^{13}\text{C}$ , our refocusing protocol would still work, but only for discrete times corresponding to the spin-echo revivals depending on the applied magnetic field, and for NV centers having their axis well aligned with the magnetic field [8, 9]. All effects taken

together, the spin distribution can be expressed as

$$f(\Delta) = \frac{w}{6\pi} \left[ \frac{1}{(\Delta - \Delta_{\text{hfs}})^2 + \frac{w^2}{4}} + \frac{1}{\Delta^2 + \frac{w^2}{4}} + \frac{1}{(\Delta + \Delta_{\text{hfs}})^2 + \frac{w^2}{4}} \right], \quad (5)$$

The corresponding characteristic width [10] can be derived:

$$\Gamma = \left( \gamma_{\perp} + \frac{w}{2} \right) \frac{(\gamma_{\perp} + \frac{w}{2})^2 + \Delta_{\text{hfs}}^2}{(\gamma_{\perp} + \frac{w}{2})^2 + \frac{1}{3}\Delta_{\text{hfs}}^2}. \quad (6)$$

We note that the free induction decay of an ensemble of identically prepared spins,  $\langle \hat{\sigma}_-^{(j)}(0) \rangle \equiv \langle \hat{\sigma}_-(0) \rangle$ , can be expressed as:

$$\begin{aligned} \langle \hat{S}_-(t) \rangle &= \sum_{j=1}^N \langle \hat{\sigma}_-^{(j)}(0) \rangle e^{-(\gamma_{\perp} + i\Delta_j)t} = N \langle \hat{\sigma}_-(0) \rangle \int_{-\infty}^{\infty} f(\Delta) e^{-(\gamma_{\perp} + i\Delta)t} d\Delta \\ &= \frac{1}{3} \langle \hat{S}_-(0) \rangle [1 + 2 \cos(\Delta_{\text{hfs}}t)] e^{-(\gamma_{\perp} + \frac{w}{2})t}. \end{aligned} \quad (7)$$

As stated in the main text, the time scale for free induction decay,  $T_2^* = \frac{2}{w}$  (taking  $\gamma_{\perp} \ll w$ ), is seen to characterize the envelope function of the modulated decay, caused by the hyperfine splitting.

## EQUATIONS OF MOTION FOR FIRST AND SECOND MOMENTS USING SUB-ENSEMBLES

With the considerations of the above section, a Hamiltonian for the physical system can be written in the frame rotating at the central spin frequency,  $\omega_s$  as:

$$\hat{H} = \hbar \Delta_{\text{cs}} \hat{a}_c^\dagger \hat{a}_c + \frac{\hbar}{2} \sum_{j=1}^N \Delta_j \hat{\sigma}_z^{(j)} + i\hbar \sqrt{2\kappa} (\beta \hat{a}_c^\dagger - \beta^* \hat{a}_c) + \hbar \sum_{j=1}^N g_j (\hat{\sigma}_+^{(j)} \hat{a}_c + \hat{\sigma}_-^{(j)} \hat{a}_c^\dagger), \quad (8)$$

where  $\Delta_{\text{cs}} = \omega_c - \omega_s$  is the detuning of the cavity-resonance frequency  $\omega_c$  from  $\omega_s$ , and  $\Delta_j = \omega_j - \omega_s$  with  $\omega_j$  being the individual spin-resonance frequencies. The sums add the contribution from the  $N$  spins residing in the volume considered. An external coherent-state field,  $\beta$ , may be used to drive the cavity field  $\hat{a}_c$  through a coupling capacitor, which gives rise to the cavity-field-decay rate  $\kappa$ . The  $c$ -number  $\beta$  is normalized such that  $|\beta|^2$  is the incoming number of photons per second.

Decay mechanisms are treated in the Markovian approximation. In our previous work [10] we employed the formalism of quantum Langevin equations, which has pedagogical appeal

for understanding the structure of Eq. (15) below. However, the present work describes more general states of the spin ensemble, in which case we prefer the approach of the Lindblad master equation. This reads:  $\frac{\partial \hat{\rho}}{\partial t} = \frac{1}{i\hbar} [\hat{H}, \hat{\rho}] + \sum_k \mathcal{D}[\hat{c}_k] \hat{\rho}$  with  $\mathcal{D}[\hat{c}_k] \hat{\rho} = -\frac{1}{2} \hat{c}_k^\dagger \hat{c}_k \hat{\rho} - \frac{1}{2} \hat{\rho} \hat{c}_k^\dagger \hat{c}_k + \hat{c}_k \hat{\rho} \hat{c}_k^\dagger$ , where  $\hat{c}_1 = \sqrt{2\kappa} \hat{a}_c$  accounts for the cavity leakage. In addition, for the  $j$ th spin a population decay with rate  $\gamma_{\parallel}$  is modeled by  $\hat{c}_{2,j} = \sqrt{\gamma_{\parallel}} \hat{\sigma}_-^{(j)}$  and phase decay with characteristic time  $\tau$  by  $\hat{c}_{3,j} = \frac{1}{\sqrt{2\tau}} \hat{\sigma}_z^{(j)}$ . Even though  $\gamma_{\parallel} = 0$  in the main text, it is included here for generality.

Our aim is to describe both the storage of weak cavity fields in the spin ensemble and the impact of very strong driving fields needed for spin-refocusing schemes. To this end we develop a formalism, which is applicable for any saturation level of the spins and which accounts for the first and second moments of relevant physical operators [Eq. (9)]. The inhomogeneous spin ensemble is divided into  $M$  sub-ensembles,  $\mathcal{M}_1, \mathcal{M}_2, \dots, \mathcal{M}_M$ , which can each be regarded as homogeneous with coupling strength  $g_m$ , spin resonance frequency  $\Delta_m$ , and containing  $N_m$  spins for  $m = 1, \dots, M$ .

Next, the dynamical variables are described in terms of the real-valued operators:

$$\begin{aligned}
\hat{X}_c &= \frac{\hat{a}_c + \hat{a}_c^\dagger}{\sqrt{2}}, \\
\hat{P}_c &= \frac{-i(\hat{a}_c - \hat{a}_c^\dagger)}{\sqrt{2}}, \\
\hat{S}_x^{(m)} &= \sum_{\mathcal{M}_m} (\hat{\sigma}_+^{(j)} + \hat{\sigma}_-^{(j)}), \\
\hat{S}_y^{(m)} &= -i \sum_{\mathcal{M}_m} (\hat{\sigma}_+^{(j)} - \hat{\sigma}_-^{(j)}), \\
\hat{S}_z^{(m)} &= \sum_{\mathcal{M}_m} \hat{\sigma}_z^{(j)}.
\end{aligned} \tag{9}$$

The  $\hat{X}_c$  and  $\hat{P}_c$  operators describe the quadratures of the cavity field with  $[\hat{X}_c, \hat{P}_c] = i$ , while the  $\hat{S}_k^{(m)}$  components correspond to twice the total spin in each sub-ensemble with  $[\hat{S}_j^{(m)}, \hat{S}_k^{(m)}] = 2i\epsilon_{jkl} \hat{S}_l^{(m)}$ . These operators are now linearized around their mean values:  $\hat{X}_c = X_c + \delta\hat{X}_c$ ,  $\hat{P}_c = P_c + \delta\hat{P}_c$ , and  $\hat{S}_k^{(m)} = S_k^{(m)} + \delta\hat{S}_k^{(m)}$  for  $k = x, y, z$ , i.e. by definition,  $\langle \delta\hat{X}_c \rangle = 0$ , etc. Using the master equation, the following mean-value equations can then be

deduced:

$$\frac{\partial X_c}{\partial t} = -\kappa X_c + \Delta_{cs} P_c - \sum_m \frac{g_m}{\sqrt{2}} S_y^{(m)} + 2\sqrt{\kappa}\beta_R, \quad (10)$$

$$\frac{\partial P_c}{\partial t} = -\kappa P_c - \Delta_{cs} X_c - \sum_m \frac{g_m}{\sqrt{2}} S_x^{(m)} + 2\sqrt{\kappa}\beta_I, \quad (11)$$

$$\frac{\partial S_x^{(m)}}{\partial t} = -\gamma_{\perp} S_x^{(m)} - \Delta_m S_y^{(m)} - \sqrt{2}g_m (S_z^{(m)} P_c + \langle \delta \hat{S}_z^{(m)} \delta \hat{P}_c \rangle), \quad (12)$$

$$\frac{\partial S_y^{(m)}}{\partial t} = -\gamma_{\perp} S_y^{(m)} + \Delta_m S_x^{(m)} - \sqrt{2}g_m (S_z^{(m)} X_c + \langle \delta \hat{S}_z^{(m)} \delta \hat{X}_c \rangle), \quad (13)$$

$$\begin{aligned} \frac{\partial S_z^{(m)}}{\partial t} &= \sqrt{2}g_m (S_x^{(m)} P_c + \langle \delta \hat{S}_x^{(m)} \delta \hat{P}_c \rangle) + S_y^{(m)} X_c + \langle \delta \hat{S}_y^{(m)} \delta \hat{X}_c \rangle \\ &\quad - \gamma_{\parallel} (S_z^{(m)} + N_m), \end{aligned} \quad (14)$$

where  $\beta_R = \text{Re}\{\beta\}$  and  $\beta_I = \text{Im}\{\beta\}$  and  $\gamma_{\perp} = \frac{1}{T_2} = \frac{1}{\tau} + \frac{\gamma_{\parallel}}{2}$ . We note that Eqs. (12)-(14) contain covariances between the spin and cavity-field operators. In practice, for all calculations in the main text, these are very small and can be omitted such that the mean-value equations by themselves form a closed set.

In total, there are  $2 + 3M$  operators to consider (two quadratures of the cavity field and three spin components for each sub-ensemble), which can be written on vector form,  $\hat{\mathbf{y}}$ , with  $\hat{X}_c$  and  $\hat{P}_c$  as the first two entries and  $\hat{S}_x^{(1)}, \hat{S}_y^{(1)}, \hat{S}_z^{(1)}, \hat{S}_x^{(2)}, \hat{S}_y^{(2)}, \hat{S}_z^{(2)}$ , etc., on the following entries. The covariance between any two of these operators,  $\hat{y}_k$  and  $\hat{y}_l$ , is defined as  $C(\hat{y}_k, \hat{y}_l) = 2\text{Re}\{\langle \delta \hat{y}_k \delta \hat{y}_l \rangle\}$ , and in particular  $C(\hat{y}_k, \hat{y}_k) = 2\text{Var}(\hat{y}_k)$ . These are grouped into a  $(2 + 3M) \times (2 + 3M)$  covariance matrix  $\boldsymbol{\gamma}$  for which the entry of the  $k$ th row and  $l$ th column is  $C(\hat{y}_k, \hat{y}_l)$ . The time-evolution of  $\boldsymbol{\gamma}$  is:

$$\frac{\partial \boldsymbol{\gamma}}{\partial t} = \mathbf{M}\boldsymbol{\gamma} + \boldsymbol{\gamma}\mathbf{M}^T + \mathbf{N}, \quad (15)$$

where the driving matrix  $\mathbf{M}$  is given by:

$$\mathbf{M} = \begin{bmatrix} \mathbf{A} & \mathbf{B}^{(1)} & \mathbf{B}^{(2)} & \dots & \mathbf{B}^{(M)} \\ \mathbf{C}^{(1)} & \mathbf{D}^{(1)} & 0 & \dots & 0 \\ \mathbf{C}^{(2)} & 0 & \mathbf{D}^{(2)} & \dots & 0 \\ \vdots & \vdots & \vdots & \ddots & \vdots \\ \mathbf{C}^{(M)} & 0 & 0 & \dots & \mathbf{D}^{(M)} \end{bmatrix}, \quad (16)$$

with

$$\begin{aligned}
\mathbf{A} &= \begin{bmatrix} -\kappa & \Delta_{\text{cs}} \\ -\Delta_{\text{cs}} & -\kappa \end{bmatrix}, & \mathbf{B}^{(m)} &= \begin{bmatrix} 0 & -\frac{g_m}{\sqrt{2}} & 0 \\ -\frac{g_m}{\sqrt{2}} & 0 & 0 \end{bmatrix}, \\
\mathbf{C}^{(m)} &= \begin{bmatrix} 0 & -\sqrt{2}g_m S_z^{(m)} \\ -\sqrt{2}g_m S_z^{(m)} & 0 \\ \sqrt{2}g_m S_y^{(m)} & \sqrt{2}g_m S_x^{(m)} \end{bmatrix}, \\
\mathbf{D}^{(m)} &= \begin{bmatrix} -\gamma_{\perp} & -\Delta_m & -\sqrt{2}g_m P_c \\ \Delta_m & -\gamma_{\perp} & -\sqrt{2}g_m X_c \\ \sqrt{2}g_m P_c & \sqrt{2}g_m X_c & -\gamma_{\parallel} \end{bmatrix}.
\end{aligned} \tag{17}$$

The noise matrix  $\mathbf{N}$  is block diagonal:

$$\begin{aligned}
\mathbf{N} &= \begin{bmatrix} \mathbf{V} & 0 & \dots & 0 \\ 0 & \mathbf{U}^{(1)} & \dots & 0 \\ \vdots & \vdots & \ddots & \vdots \\ 0 & 0 & \dots & \mathbf{U}^{(M)} \end{bmatrix}, & \mathbf{V} &= \begin{bmatrix} 2\kappa & 0 \\ 0 & 2\kappa \end{bmatrix}, \\
\mathbf{U}^{(m)} &= \begin{bmatrix} 4\gamma_{\perp} N_m & 0 & 2\gamma_{\parallel} S_x^{(m)} \\ 0 & 4\gamma_{\perp} N_m & 2\gamma_{\parallel} S_y^{(m)} \\ 2\gamma_{\parallel} S_x^{(m)} & 2\gamma_{\parallel} S_y^{(m)} & 4\gamma_{\parallel} (S_z^{(m)} + N_m) \end{bmatrix}.
\end{aligned} \tag{18}$$

The above derivation of Eq. (15) follows from the master equation with the approximation that moments of order higher than two have been neglected. Since second moments have proved negligible in Eqs. (12)-(14), it can be expected in succession that moments of order higher than two are also negligible and the approximation is well justified.

Note that both  $\mathbf{M}$  and  $\mathbf{N}$  contain mean values, and hence the second-moment equation do *not* form a closed set. However, if all spins are close to the ground or excited state,  $S_z^{(m)} \approx \pm N_m$ , the  $\hat{S}_z^{(m)}$ -operators are effectively removed from the dynamics and the first- and second-moment equations reduce to the linear, de-coupled sets published in [10].

## IMPLEMENTING THE QUANTUM MEMORY PROTOCOL

In the following the timing details of the quantum memory protocol are stated. The schematic setup shown in Fig. 2(a) of the main text is presented in further detail in Fig. 5.

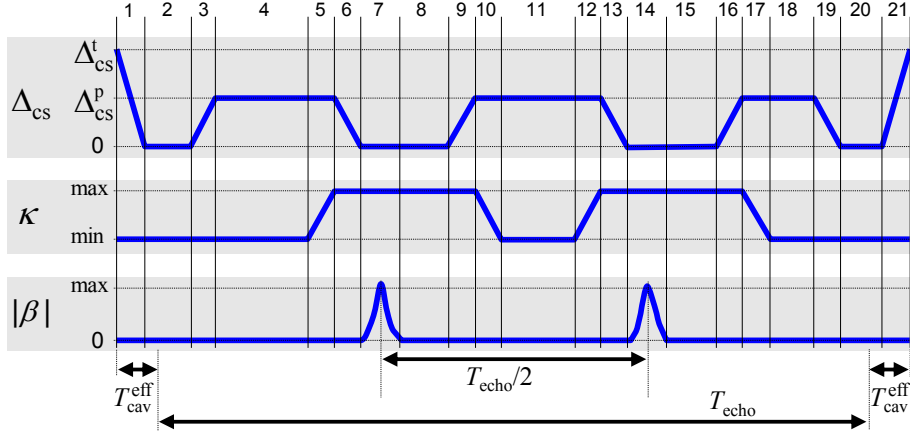


FIG. 5. The detailed pulse sequence (not to scale) showing the evolution of the external control parameters,  $\Delta_{cs}$ ,  $\kappa$ , and  $\beta$ .  $T_{cav}^{eff}$  marks the time, which the quantum state spends *effectively* in the cavity.

The protocol sequence consists of 21 parts, and the duration of the  $j$ th part is denoted by  $T_j$ . There are three important cavity-frequency detunings in the protocol. (1) At the “target frequency”  $\Delta_{cs}^t = 2\pi \cdot 100$  MHz the cavity field is given to us for storage or we must deliver the state at this frequency after memory retrieval, (2) at resonance  $\Delta_{cs} = 0$  the spin-cavity interaction is effective, and (3) at  $\Delta_{cs}^p = 2\pi \cdot 50$  MHz the cavity is parked when the spin-cavity interaction needs to be turned off (in safe distance from the target frequency). Maintaining a chirp rate of  $2\pi \cdot 10$  MHz/ns, we denote by  $T_{\Delta}^p = 5$  ns the time of the chirp  $0 \rightarrow \Delta_{cs}^p$  and by  $T_{\Delta}^t = 10$  ns the time of the chirp  $0 \rightarrow \Delta_{cs}^t$  (equal to  $T_{chirp}$  in the main text). Hence, in the protocol we take  $T_1 = T_{21} = T_{\Delta}^t$  and  $T_3 = T_6 = T_9 = T_{13} = T_{16} = T_{19} = T_{\Delta}^p$ . The cavity-field decay rate  $\kappa$  is also varied linearly in time with a duration taken to be  $T_5 = T_{10} = T_{12} = T_{17} \equiv T_{\kappa} = 10$  ns.

The duration  $T_2 = T_{20} = T_{swap} = 73.7$  ns of the storage and retrieval is determined numerically by the condition that the cavity field amplitude  $|\langle \hat{a}_c \rangle|$  is minimized after part 3 of the sequence. The “ideal” time of  $\frac{\pi}{2g_{ens}} = 71.4$  ns is modified due to cavity decay, inhomogeneous broadening, and the fact that the information transfer extends slightly into parts 1 and 3 (or parts 19 and 21).

The duration of the external driving pulses are chosen to be  $T_7 = T_{14} \equiv T_{\pi} = 1$   $\mu$ s. The desired intra-cavity-field mean value  $a_c$  is obtained by tailoring the external driving field  $\beta$  as follows: Solve first Eqs. (12)-(14) with  $X_c$  and  $P_c$  given by the desired  $a_c$  (the secant

hyperbolic pulse stated in the main text) and with initial conditions  $S_x^{(m)} = S_y^{(m)} = 0$  and  $S_z^{(m)} = \pm N_m$  where plus and minus are chosen for the second and first  $\pi$  pulse, respectively. Second, the external  $\beta$  can be found from re-arranging Eqs. (10) and (11) [we write it on complex form]:

$$\beta = \frac{1}{\sqrt{2\kappa}} \left[ \frac{\partial a_c}{\partial t} + (\kappa + i\Delta_{cs})a_c + i \sum_m g_m S_-^{(m)} \right], \quad (19)$$

where  $S_-^{(m)} = \frac{S_x^{(m)} - iS_y^{(m)}}{2}$  is the solution from the first step. The first term  $\frac{\partial a_c}{\partial t}$  accounts for the finite response time of the cavity while the third term including  $S_-^{(m)}$  describes the reaction field from the magnetic dipole moments of the spin ensemble.

After each inversion pulse the mean values of the cavity field quadratures,  $X_c$  and  $P_c$ , and of the transverse spin components,  $S_x$  and  $S_y$ , will inevitably contain small, non-zero values due to a non-perfect inversion process. These mean values must relax to appropriate levels before the cavity parameters can be changed (due to saturation effects in the cavity-tuning circuitry), which is ensured by (parts 8 and 15) during the additional time on resonance,  $T_8 = T_{15} \equiv T_{\text{res}} = 1 \mu\text{s}$ . Moreover, these mean values together with the possible excited-state excess variance must be reduced even further: If the stored cavity field was the vacuum state, the spin-mode coupled to the cavity must also be effectively in the vacuum state at the time of the primary spin echo in part 11 and at the time of the memory retrieval. Otherwise, any stored quantum state will be distorted. Specifically, for the second inversion pulse the time  $T_{15} + \dots + T_{19}$  must be long enough for the mean values to decay and the time  $T_{16} + \dots + T_{19}$  must be long enough for the excess noise to decay (a similar condition applies after the first inversion pulse).

Since relaxation is required after both the first and second inversion pulses, it is convenient to arrange the sequence such that the primary spin echo occurs right in the middle of the inversion pulses. This is obtained when the total time before the first inversion pulse equals the duration after the second,  $T_1 + \dots + T_6 = T_{15} + \dots + T_{21}$ , which with the choices above reduces to:

$$T_4 = T_{\text{res}} + T_{18}. \quad (20)$$

Next, the duration  $T_{\text{echo}}$ , between the *effective* focus points of the reversible spin dephasing process, must fulfill (see bottom part of Fig. 5):

$$T_{\text{echo}} = T_{\text{mem}} - 2T_{\text{cav}}^{\text{eff}} = 2 \sum_{j=7}^{13} T_j, \quad (21)$$

where the last expression is equal to twice the time between the inversion pulses. Finally, the total memory time  $T_{\text{mem}}$  is given by us:

$$T_{\text{mem}} = \sum_{j=1}^{21} T_j. \quad (22)$$

The above expressions (20)-(22) present four equations with the four unknowns  $T_4$ ,  $T_{11}$ ,  $T_{18}$ , and  $T_{\text{echo}}$ . After some algebra we find:

$$T_{11} = \frac{T_{\text{mem}}}{2} - 2T_{\Delta}^{\text{p}} - 2T_{\kappa} - T_{\pi} - T_{\text{res}} - T_{\text{cav}}^{\text{eff}}, \quad (23)$$

$$T_{18} = \frac{T_{\text{mem}}}{4} - T_{\Delta}^{\text{t}} - 2T_{\Delta}^{\text{p}} - T_{\kappa} - \frac{T_{\pi}}{2} - T_{\text{res}} - T_{\text{swap}} + \frac{T_{\text{cav}}^{\text{eff}}}{2}, \quad (24)$$

and  $T_4$  and  $T_{\text{echo}}$  follow immediately from Eqs. (20) and (21). The effective time  $T_{\text{cav}}^{\text{eff}}$  can be calculated by choosing some initial guess, e.g. halfway into part 2, and extending  $T_{18}$  such that the time  $t_{\text{revival}}$  of the spin revival occurs within part 18. Then the correct value follows:  $T_{\text{cav}}^{\text{eff}} = t_{\text{revival}} - T_{\text{echo}}$ .

The multi-mode version of the protocol discussed around Fig. 4 in the main text has been simulated as follows: After the initial storage (parts 1-3) and a waiting time of  $0.19 \mu\text{s}$ , the cavity is chirped to the target frequency  $\Delta_{\text{cs}}^{\text{t}}$  and the cavity field is then *replaced* by a new coherent field ( $\langle \delta \hat{X}_c^2 \rangle = \langle \delta \hat{P}_c^2 \rangle \rightarrow \frac{1}{2}$ , correlations between the cavity field and each sub-ensemble of spins is set to zero, while spin-spin correlations are maintained). This new quantum state is then stored in complete analogy to the first input state. The retrieval is just the reverse process, and when the cavity reaches the target frequency  $\Delta_{\text{cs}}^{\text{t}}$ , the cavity is reset to the vacuum state. This protocol models a perfect, infinitely fast swap between the cavity and some “target system”, which holds the unknown quantum state in the storage part of the protocol and which is prepared in its ground state at the point of retrieval. In addition, we used a cavity  $Q$ -parameter of  $10^3$  between these pulses to facilitate a lower cross talk. In the simulation shown in Fig. 4 of the main text, the gain factor is 0.80, being lower by the factor  $e^{-\gamma_{\perp}(2 \mu\text{s})}$  due to the extra memory time as compared to the case of homogeneous coupling strengths in Fig. 3, and the variance is maintained at  $2\sigma^2 = 1.02$ . As mentioned in the summary of the main text, the experimentally feasible case with inhomogeneous coupling strength and  $P_{\text{peak}} = 100 \mu\text{W}$  presents non-classical storage capabilities with  $T_{\text{mem}}$  up to  $69 \mu\text{s}$ , which can be deduced using the fact that an additional memory time  $\Delta T$  will decrease the gain by the factor  $e^{-\Delta T/T_2}$ . Using the pulse separation of  $0.29 \mu\text{s}$  as in Fig. 4 the protocol will accommodate 100 pulses when  $T_{\text{mem}} = 69 \mu\text{s}$ .

- 
- [1] P. Neumann, R. Kolesov, V. Jacques, J. Beck, J. Tisler, A. Batalov, L. Rogers, N. B. Manson, G. Balasubramanian, F. Jelezko, and J. Wrachtrup, *New J. Phys.* **11**, 013017 (2009).
- [2] R. N. Simons, *Coplanar waveguide circuits, components, and systems* (John Wiley & Sons, Inc., New York, 2001).
- [3] A. Blais, R. Huang, A. Wallraff, S. M. Girvin, and R. J. Schoelkopf, *Phys. Rev. A* **69**, 062320 (2004).
- [4] Y. Kubo, F. R. Ong, P. Bertet, D. Vion, V. Jacques, D. Zheng, A. Dreau, J. F. Roch, A. Auffeves, F. Jelezko, J. Wrachtrup, M. F. Barthe, P. Bergonzo, and D. Esteve, *Phys. Rev. Lett.* **105**, 140502 (2010).
- [5] S. Felton, A. M. Edmonds, M. E. Newton, P. M. Martineau, D. Fisher, D. J. Twitchen, and J. M. Baker, *Phys. Rev. B* **79**, 075203 (2009).
- [6] J. A. van Wyk, E. C. Reynhardt, G. L. High, and I. Kiflawi, *J. Phys. D: Appl. Phys.* **30**, 1790 (1997).
- [7] Y. Kubo, C. Grezes, A. Dewes, T. Umeda, J. Isoya, H. Sumiya, N. Morishita, H. Abe, S. Onoda, T. Ohshima, V. Jacques, A. Dréau, J.-F. Roch, I. Diniz, A. Auffeves, D. Vion, D. Esteve, and P. Bertet, *Phys. Rev. Lett.* **107**, 220501 (2011).
- [8] P. L. Stanwix, L. M. Pham, J. R. Maze, D. Le Sage, T. K. Yeung, P. Cappellaro, P. R. Hemmer, A. Yacoby, M. D. Lukin, and R. L. Walsworth, *Phys. Rev. B* **82**, 201201(R) (2010).
- [9] J. R. Maze, J. M. Taylor, and M. D. Lukin, *Phys. Rev. B* **78**, 094303 (2008).
- [10] B. Julsgaard and K. Mølmer, *Phys. Rev. A* **86**, 063810 (2012).